Lee et al. *NPG Asia Materials* (2020) 12:82
https://doi.org/10.1038/s41427-020-00272-x

NPG Asia Materials

ARTICLE Open Access

Understanding filamentary growth and rupture by Ag ion migration through single-crystalline 2D layered $CrPS_4$

Mi Jung Lee[1], Sung-Hoon Kim[2,3], Sangik Lee[1], Chansoo Yoon[1], Kyung-Ah Min[4], Hyunsoo Choi[4], Suklyun Hong[4], Sungmin Lee[5,6], Je-Geun Park[5,6], Jae-Pyoung Ahn[2] and Bae Ho Park[1]

Abstract

Memristive electrochemical metallization (ECM) devices based on cation migration and electrochemical metallization in solid electrolytes are considered promising for neuromorphic computing systems. Two-dimensional (2D) layered materials are emerging as potential candidates for electrolytes in reliable ECM devices due to their two-dimensionally confined material properties. However, electrochemical metallization within a single-crystalline 2D layered material has not yet been verified. Here, we use transmission electron microscopy and energy-dispersive X-ray spectroscopy to investigate the resistive switching mechanism of an ECM device containing a single-crystalline 2D layered $CrPS_4$ electrolyte. We observe the various conductive filament (CF) configurations induced by an applied voltage in an Ag/$CrPS_4$/Au device in the initial/low-resistance/high-resistance/breakdown states. These observations provide concrete experimental evidence that CFs consisting of Ag metal can be formed inside single-crystalline 2D layered $CrPS_4$ and that their configuration can be changed by an applied voltage. Density functional theory calculations confirm that the sulfur vacancies in single-crystalline $CrPS_4$ can facilitate Ag ion migration from the active electrode layer. The electrically induced changes in Ag CFs inside single-crystalline 2D layered $CrPS_4$ raise the possibility of a reliable ECM device that exploits the properties of two-dimensionally confined materials.

Introduction

Resistive random access memory (RRAM) has attracted much attention due to its excellent performance characteristics (such as low power consumption and excellent scalability) and simple structure[1–3]. Electrochemical metallization (ECM) cells are one of the most promising types of RRAM devices among the numerous emerging nonvolatile memory technologies; they hold the potential to facilitate novel memory or computing architectures that can circumvent the von Neumann bottleneck[3–6]. ECM devices operate using the migration of cations originating from an active metal electrode and electrochemical metallization, and the resistance state changes through the formation and dissolution of the conducting bridge in the electrolyte. Typically, an ECM cell features a simple metal–electrolyte (insulator)–metal structure, in which a solid electrolyte layer is sandwiched between an active metal electrode (Cu or Ag) and an inert metal electrode (Pt or Au). The ECM cell can be switched between a low-resistance state (LRS) and a high-resistance state (HRS) through the application of an external voltage. According to the conventional ECM mechanism, when a positive bias is applied to the active metal electrode, the electrochemically oxidized cations drift through the solid electrolyte layer and are reduced with the help of electrons provided by the inert metal cathode[2,6]. This process leads to the formation of conductive filaments (CFs), which lower the device resistance state in a process

Correspondence: Jae-Pyoung Ahn (jpahn@kist.re.kr) or
Bae Ho Park (baehpark@konkuk.ac.kr)
[1]Department of Physics, Konkuk University, Seoul 05029, Korea
[2]Advanced Analysis Center, Korea Institute of Science and Technology, Seoul 02792, Korea
Full list of author information is available at the end of the article
These authors contributed equally: Mi Jung Lee, Sung-Hoon Kim

© The Author(s) 2020

Open Access This article is licensed under a Creative Commons Attribution 4.0 International License, which permits use, sharing, adaptation, distribution and reproduction in any medium or format, as long as you give appropriate credit to the original author(s) and the source, provide a link to the Creative Commons license, and indicate if changes were made. The images or other third party material in this article are included in the article's Creative Commons license, unless indicated otherwise in a credit line to the material. If material is not included in the article's Creative Commons license and your intended use is not permitted by statutory regulation or exceeds the permitted use, you will need to obtain permission directly from the copyright holder. To view a copy of this license, visit http://creativecommons.org/licenses/by/4.0/.

referred to as "SET switching". When the bias polarity is reversed, an electrochemical process at a high local temperature—induced by the Joule heating effect—facilitates the diffusion of cations into the surrounding material under a concentration gradient, which dissolves the CFs and switches the device to an HRS in a process referred to as "RESET switching"[6–8]. This characteristic has attracted widespread attention from academic researchers, who have identified the potential of this technology for use in memristors, reconfigurable logic/analog circuitry, and neuromorphic application systems[9–13]. Because ECM devices operate on the basis of ionic carriers and their resistive switching (RS) relies upon the ion movements within the electrolyte, they have a particular advantage in mimicking biological synapses due to the similarity of the operation principles[14–16].

Moreover, ECM kinetics have been found to be highly electrolyte dependent, leading to diverse filament growth modes and structures[17,18]. However, the random and frequent migration of cations from the active metal electrode into the electrolyte layer may result in poor uniformity, inferior retention of the LRS, and deterioration of reliability in ECM devices. Therefore, it is necessary to investigate solid electrolyte materials that can localize and regulate the migration of cations on the nanoscale level to further improve the RS performance of ECM devices.

Because of the properties of two-dimensionally confined materials, two-dimensional (2D) layered materials such as graphene, transition metal dichalcogenides, and $TMPS_x$ (TM = transition metal) are emerging as potential candidates for solid electrolytes in reliable ECM devices[19–23]. Understanding the fundamental mechanisms of RS behaviors in new switching materials is crucial for designing and optimizing the associated devices and facilitates theoretical research on nanoscale materials. Extensive efforts have already been made to elucidate the RS mechanisms of various 2D layered materials. 2D layered material-based memory devices typically show that RS is controlled by the formation and rupture of CFs consisting of oxygen vacancies in the oxide layers formed on the material surfaces[21]. Otherwise, filamentary paths can be formed along the grain boundaries in polycrystalline 2D sheets, which can be grown by a chemical vapor deposition method[23,24]. However, neither the surface oxides nor grain boundaries show the properties of two-dimensionally confined materials, and thus, they are not expected to enhance the RS performance of 2D layered materials. To date, the migration of cations within a single-crystalline 2D layered material electrolyte in an ECM device structure has not been explored.

In this work, we report the formation and rupture of CFs through Ag ion migration inside a single-crystalline 2D van der Waals (vdW) solid electrolyte material within an ECM device structure. Various CF configurations—induced by applied voltage in an Ag/$CrPS_4$/Au device in the initial/LR/HR/breakdown states—are directly observed using ex situ transmission electron microscopy (TEM) and energy-dispersive X-ray spectroscopy (EDS). This study provides clear experimental evidence that CFs consisting of Ag can be formed inside single-crystalline 2D layered $CrPS_4$, and their configuration can be changed by the applied voltage. Density functional theory (DFT) calculations also confirm that Ag ion migration from the active electrode layer to the sulfur vacancies of the $CrPS_4$ layer is an energetically favorable process. The electrically induced change in Ag CFs inside single-crystalline $CrPS_4$ raises the possibility of a reliable ECM device exploiting the properties of two-dimensionally confined materials.

Materials and methods

Fabrication of ECM devices with $CrPS_4$ electrolytes

Ag/$CrPS_4$/Au cross-point devices were fabricated on SiO_2/Si substrates. Single-crystalline $CrPS_4$ was grown from high-purity Cr, P, and S powders using a chemical vapor transport method. Mechanically exfoliated $CrPS_4$ layers on poly(methyl methacrylate) were transferred onto the bottom Au electrodes with a width of 3 μm, which were deposited on SiO_2 substrates. The top Ag electrodes with ~110-nm thickness and 3-μm width were deposited via electron-beam evaporation. The electrodes were patterned using electron-beam lithography and a lift-off process. To test metal migration into bulk $CrPS_4$, Ag or Cr top layers were deposited onto bulk $CrPS_4$ on SiO_2 substrates using electron-beam evaporation. The detailed process has been previously reported in the literature[22].

Analysis of electrical properties

The *I*–*V* curves of the ECM devices were obtained by sweeping DC bias voltages between the top Ag and bottom Au electrodes (at room temperature) using a semiconductor parameter analyzer (Agilent 4156B), for which the bottom electrode was grounded.

Analysis of microstructures and atomic arrangements

The microstructure of the Ag/$CrPS_4$/Au device in each resistance state was analyzed by a TEM (Talos F200X, Thermo Fisher, USA) equipped with Super-X EDS, including four 200 keV silicon drift detectors to monitor the structural and compositional changes. Wedge-shaped samples for TEM analysis were prepared with a dual-beam focused ion beam (Helios NanoLab 600, Thermo Fisher, USA) system using Ga^+ ions at 30 keV through the backside milling method.

Theoretical calculation

We performed the DFT calculations under a generalized gradient approximation (GGA) for exchange-correlation

(xc) functionals[25,26], implemented in the Vienna ab initio simulation package[27,28]. The kinetic energy was set to 400 eV, and projector augmented wave potentials[29,30] were used to describe the electron–ion interactions. For the vdW corrections, Grimme's DFT-D3 method[31]—based on a semiempirical GGA-type theory—was adopted. In calculations, we used supercells for mono- and bilayer $CrPS_4$ with an X-antiferromagnetic phase, which was the ground state of bulk $CrPS_4$[32,33] (Supporting Information, Figure S1 and Table S1): mono- and bilayer $CrPS_4$ were constructed from the bulk with optimized magnetic ordering and lattice parameters. To describe the vacancy defects inside $CrPS_4$, we investigated several configurations with vacancy defects in $CrPS_4$ by obtaining the vacancy formation energy (E_{VFE}) per unit cell: $E_{VFE} = E_{defective\,CrPS_4} - \left(\frac{n-n_d}{n}\right)E_{CrPS_4}$, where $E_{defective\,CrPS_4}$ and E_{CrPS_4} are the total energies of defective and defect-free $CrPS_4$, respectively. Here, n is the total number of atoms for defect-free $CrPS_4$, while n_d is the number of defect atoms in defective $CrPS_4$. As a result, we obtained favorable configurations of $CrPS_4$ with mono- and divacancy defects in S atoms. On the other hand, the energy barrier for the penetration of Ag atoms into $CrPS_4$ was calculated by the nudge elastic band (NEB) method. Within the supercells of monolayer and bilayer $CrPS_4$ with lateral cell parameters $a = 10.98$ and $b = 7.45$, two kinds of pathways for the Ag atom were considered: the migration of Ag atoms through monolayer $CrPS_4$ and that between adjacent $CrPS_4$ layers. All atomic coordinates were optimized until the Hellmann–Feynman forces were <0.2 eV/Å. For the Brillouin-zone integration, we used a (2 × 3 × 1) grid in the gamma-centered scheme.

Results and discussion

Figure 1a, b displays the basic structure and cross-sectional TEM image of a $CrPS_4$-based ECM device. The ECM device is fabricated on a SiO_2/Si substrate and consists of four layers: Au (top electrode, TE) with a thickness of 30–50 nm; Ag (active TE) with a thickness of 150–200 nm; $CrPS_4$ (solid electrolyte) with a thickness of 150–200 nm; and Au (bottom electrode, BE) with a thickness of 50–100 nm. The cross-sectional TEM image in Fig. 1b reveals that all layers of the device were stacked with well-defined and clear interfaces. The metal electrodes were fabricated using electron-beam (e-beam) lithography, e-beam evaporation, and lift-off processes. The flakes of the 2D-layered $CrPS_4$ (synthesized by a chemical vapor transport method) were mechanically exfoliated and aligned on the patterned Au BE using a transfer method. Although this device had not been exposed to additional stimuli (such as heat and electricity) after fabrication, the upper part of the $CrPS_4$ layer (near the Ag active TE) shows brighter contrast than the other regions of the $CrPS_4$ layer in Fig. 1b. Because samples prepared by a focused ion beam can be contaminated by debris from the materials in the upper part during milling, the bright materials observed in the $CrPS_4$ layer can be regarded as debris from the Ag layer. To avoid these unintended artifacts in the $CrPS_4$ layer, all samples—including the device in Fig. 1a—were prepared using the backside milling method (Supporting Information, Figure S2). Because the bright region is located near the Ag active TE, the bright contrast can be attributed to the Ag atoms infiltrating into the $CrPS_4$ layer. The detailed ionic distributions of this initial state are described in Fig. 2.

To evaluate the performance of the device, a direct current (DC) voltage was applied to the Au/Ag TE while the Au BE was grounded, as shown in Fig. 1c. Despite the bright contrast in the TEM image of the upper part of $CrPS_4$ in the initial state, this initial state shows high resistance values of $\sim 10^{12}\,\Omega$. An electroforming process under a compliance current of 0.1 mA was required to induce initial RS behavior followed by reproducible RS. The electroforming process for Au/Ag/$CrPS_4$/Au devices was achieved by applying a high voltage (≈+12 V), under which the conductance suddenly increase; this is referred to as $V_{forming}$ (green square in Fig. 1c). After electroforming, the resistance state of the $CrPS_4$ layer could be easily and reversibly converted between an LRS and HRS with the help of very low switching voltages. Through RESET switching, which occurred at $V_{reset} \approx -0.33$ V, the device abruptly returned to an HRS, and the current flow was considerably suppressed (red square in Fig. 1c). Subsequently, when a positive bias exceeding $V_{set} \approx 0.33$ V was applied to the Ag TE, the device was switched to an LRS, and a high current flow was permitted (blue square in Fig. 1c). In addition, the device exhibited good retention and endurance characteristics (Supporting Information, Figure S3). This process has been observed in dozens of devices and can also be found in previously reported literature[22].

Because the $CrPS_4$ layer in the initial state shows a bright area in the TEM image in Fig. 1b, it was first necessary to verify the crystallinity of the $CrPS_4$ used in this device. We analyzed the atomic arrangement of a mechanically exfoliated $CrPS_4$ flake without deposition of electrode materials using TEM (Fig. 1d). The $CrPS_4$ flake (size: ~20 μm; thickness ~200 nm) exhibited a single-crystalline monoclinic structure (C_{121}). The surface normal direction through the thickness was in the [001] direction.

In most ECM devices, the transition mechanism between LRS and HRS is known to be the formation and rupture of CFs inside the insulator. A previous report[22] suggested that higher switching voltages were required in an ECM device with a thicker $CrPS_4$ layer due to both the migration of Ag ions in the thicker $CrPS_4$ layer and the formation of longer CFs. In addition, it was argued that

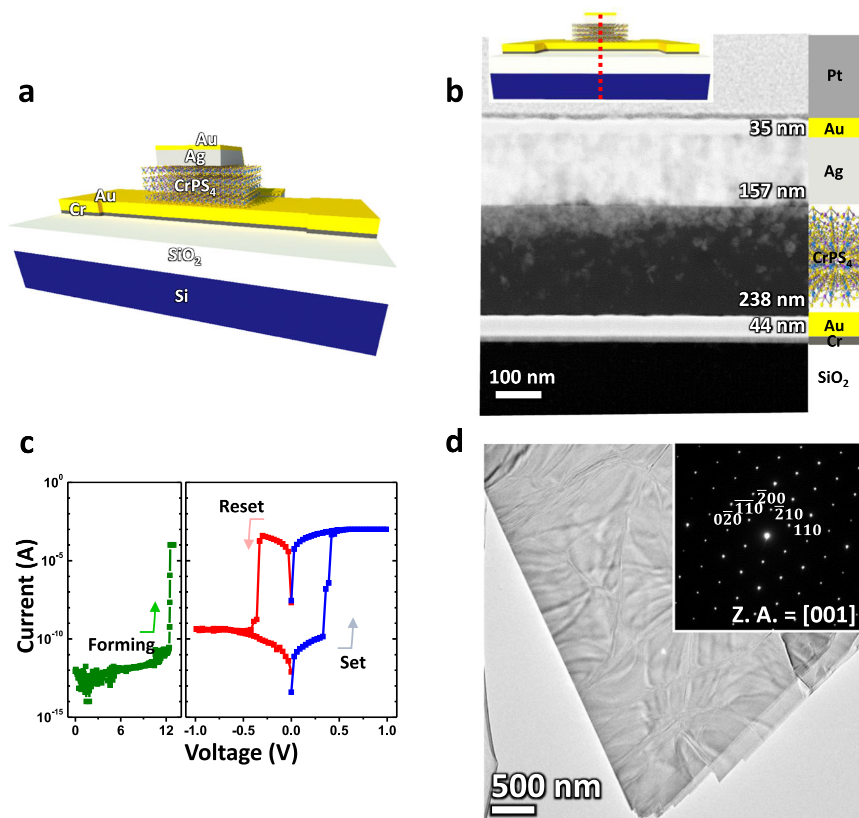

Fig. 1 Structure and resistive switching (RS) characteristics of an electrochemical metallization (ECM) device with a single-crystalline $CrPS_4$ electrolyte. a schematic diagram and **b** cross-sectional transmission electron microscopy (TEM) image. **c** RS characteristics of an ECM device with a single-crystalline $CrPS_4$ electrolyte. **d** TEM image of a single-crystalline $CrPS_4$ flake. The inset of (**d**) shows its fast Fourier transform pattern.

both LRS and HRS could be maintained for a long time due to the stably formed filaments. The behaviors of these filaments are attributable to the oxidation and reduction of migrated ions originating from the active TE materials (such as Ag and Cu) in the solid electrolyte[6]. Therefore, we investigated the behavior of Ag ions in the $CrPS_4$ layer, which is the solid electrolyte in our device. To understand the mechanism underlying the RS characteristics of $CrPS_4$, we analyzed four cross-sectional samples of the Au/Ag/$CrPS_4$/Au devices in their initial state, LRS, HRS, and breakdown state using TEM and observed the formation and rupture behaviors of filaments in $CrPS_4$. Because the chemical composition of $CrPS_4$ is not identical in all samples, the quantitative values of atomic compositions are not suitable for accurately studying the changes occurring during cyclic tests. Therefore, we compared the trends in the compositional change through the thickness direction for these samples. We analyzed the composition of the whole device to determine the changes in average composition and distribution through the thickness. Figure 2 shows the high-angle annular dark-field scanning TEM (HAADF STEM) images, EDS mapping images, and line profiles indicating compositional changes through the thickness direction of the Au/Ag/$CrPS_4$/Au devices in the initial state, LRS, and HRS. In particular, devices in stable HRS and LRS were obtained after more than 10 cycles of DC voltage sweeps.

Ag atoms were detected in the $CrPS_4$ layer near the upper interface of the device in the initial state (Fig. 2a). To verify the reason for the infiltration of Ag, we analyzed a Ag/$CrPS_4$ sample obtained halfway through the process of fabricating a Au/Ag/$CrPS_4$/Au device (Supporting Information, Figure S4). It was found that Ag atoms could infiltrate into the $CrPS_4$ layer during the e-beam deposition process without any additional electrical or thermal stimulation. After a positive bias was applied to an Au/Ag/$CrPS_4$/Au device, the device switched to an LRS, and Ag was detected evenly across the whole $CrPS_4$ layer, although the CFs were not clearly defined (Fig. 2b). After a negative bias was applied to an Au/Ag/$CrPS_4$/Au device, the device switched to an HRS, and the concentration of Ag significantly decreased across the whole $CrPS_4$ layer (Fig. 2c). A considerable number of Ag atoms remained at the interface between the Ag TE and $CrPS_4$ layer, which was similar to the initial state. In contrast, Ag atoms also remained at the interface between $CrPS_4$ and the Au BE of the device in the HRS.

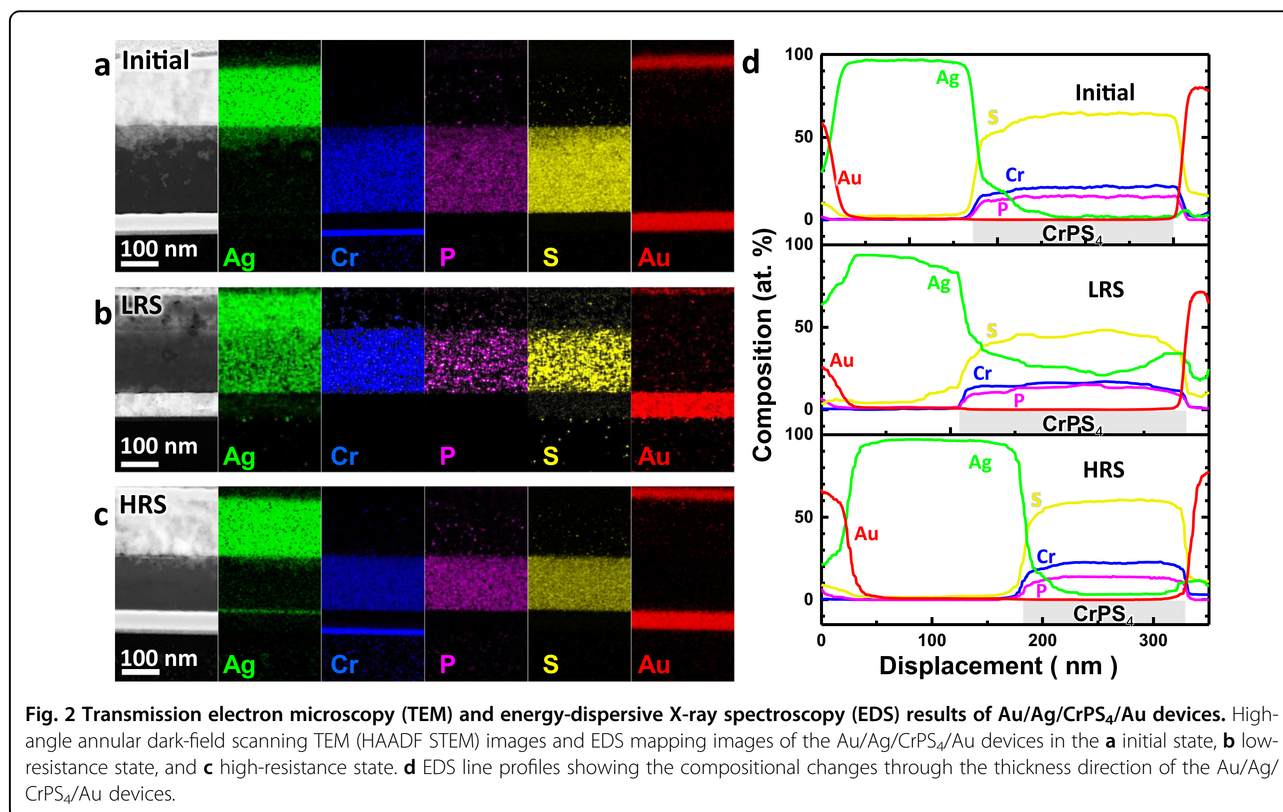

Fig. 2 Transmission electron microscopy (TEM) and energy-dispersive X-ray spectroscopy (EDS) results of Au/Ag/$CrPS_4$/Au devices. High-angle annular dark-field scanning TEM (HAADF STEM) images and EDS mapping images of the Au/Ag/$CrPS_4$/Au devices in the **a** initial state, **b** low-resistance state, and **c** high-resistance state. **d** EDS line profiles showing the compositional changes through the thickness direction of the Au/Ag/$CrPS_4$/Au devices.

To measure the compositional changes through the thickness direction, we analyzed the EDS line profile, which showed the change in normalized atomic composition from the TE to the BE (Fig. 2d). The concentration of Ag in the $CrPS_4$ layer in the initial state rapidly decreased from 22 at.% at the Ag/$CrPS_4$ interface to 1.8 at.% at the center of the layer. The average Ag concentration in the entire initial state $CrPS_4$ layer was 4.6 at.%. Despite the absence of additional stimulation, a considerable quantity of Ag can infiltrate into the surface of the $CrPS_4$ layer in the initial state. Because electroforming is the first migration process of Ag from the Ag TE to the Au BE in single-crystalline $CrPS_4$, a large quantity of energy is required to form the first Ag filament. It is anticipated that the initial presence of Ag in $CrPS_4$ may help CFs form during the electroforming process with relatively low energy consumption. Furthermore, these Ag atoms present in the initial state can induce forming-free RS behaviors[22], which might be useful in reducing power consumption and improving the uniformity of switching behavior[34].

After the device was switched to LRS, the concentration of Ag increased to 50 at.% at the Ag/$CrPS_4$ interface and to 20 at.% at the center of the $CrPS_4$ layer. The average Ag concentration in the whole $CrPS_4$ layer also increased to 28.5 at.%. After the device was switched to HRS, the concentration of Ag decreased to 20 at.% at the Ag/$CrPS_4$ interface and to 3.3 at.% at the center of the $CrPS_4$ layer. The compositional distribution of Ag in the HRS was similar to that observed in the initial state. To confirm the compositional changes of $CrPS_4$, we compared the ratios of Cr, P, and S in the $CrPS_4$ layers of all devices. The ratios of Cr, P, and S in the $CrPS_4$ layers were 1:0.7:3.2 (initial state), 1:0.8:2.9 (LRS), and 1:0.6:2.7 (HRS). Because the initial composition of each device differs, direct comparisons of these values are not suitable. However, we observed decreasing trends in the S concentration after electrical stimulation compared to the initial state. These findings imply that repetitive electrical stimulation induces more S vacancies, which may facilitate the movement of Ag ions in the $CrPS_4$ layer.

To confirm the morphology of Ag filaments and its effect on the crystallinity of the $CrPS_4$ layer, we obtained scanning TEM (STEM) and high-resolution TEM (HRTEM) images of the $CrPS_4$ layers (Fig. 3). From the low-magnification images in Fig. 2b, we can assess the concentration and distribution of Ag in the $CrPS_4$ layer; however, we cannot distinguish the configuration of filaments. In the STEM images of the $CrPS_4$ layer in the LRS, it can be seen that the Ag filaments were clearly defined in $CrPS_4$ (Fig. 3a). Ag ions in $CrPS_4$ at the LRS heavily accumulated in the region near the Ag/$CrPS_4$ interface. These Ag ions moved to the BE and formed filaments to connect the TE and BE. Because this image

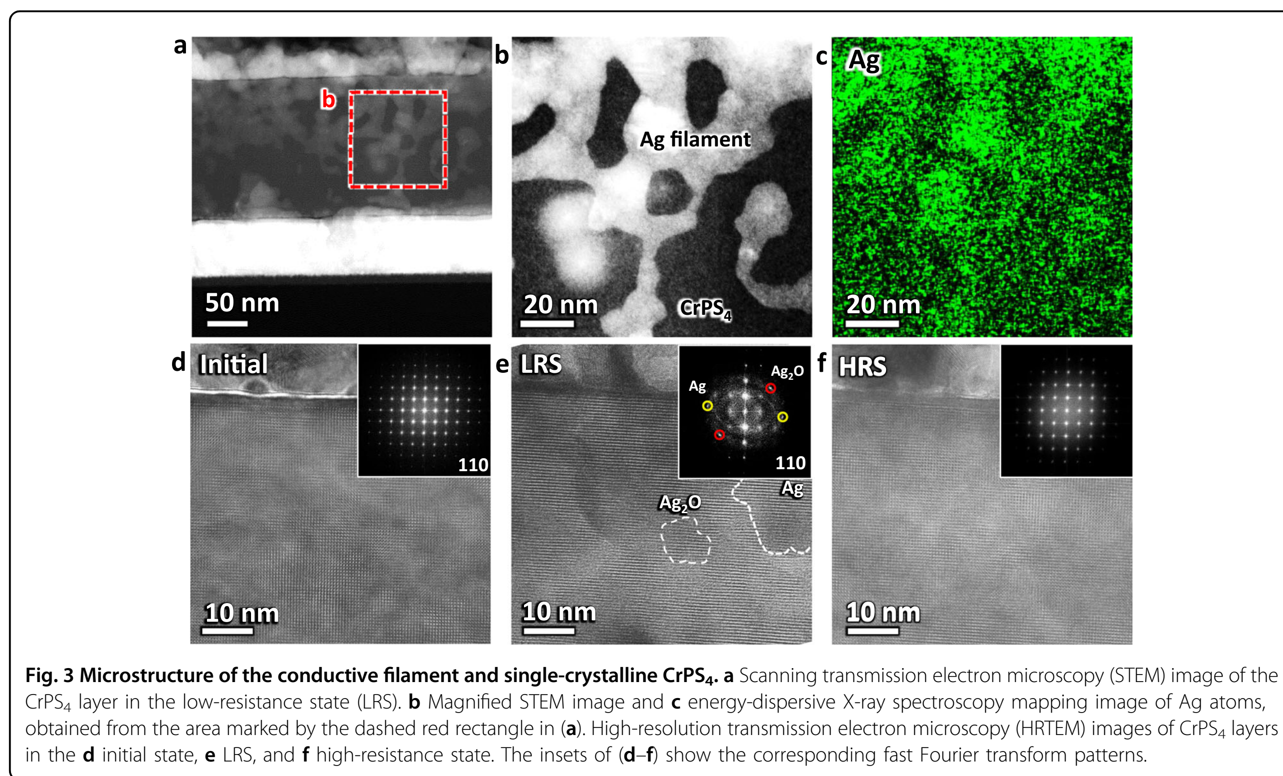

Fig. 3 Microstructure of the conductive filament and single-crystalline $CrPS_4$. **a** Scanning transmission electron microscopy (STEM) image of the $CrPS_4$ layer in the low-resistance state (LRS). **b** Magnified STEM image and **c** energy-dispersive X-ray spectroscopy mapping image of Ag atoms, obtained from the area marked by the dashed red rectangle in (**a**). High-resolution transmission electron microscopy (HRTEM) images of $CrPS_4$ layers in the **d** initial state, **e** LRS, and **f** high-resistance state. The insets of (**d**–**f**) show the corresponding fast Fourier transform patterns.

represents a small volume of the whole device, only one filament, consisting of many branches connecting the TE and BE, is visible. To distinguish the Ag filaments more clearly from the $CrPS_4$ layer, we magnified the area marked by the dashed red rectangle in Fig. 3a (Fig. 3b) and analyzed the EDS map of Ag atoms (Fig. 3c). The concentration of Ag at the filaments was higher than that in the $CrPS_4$ matrix layer. To confirm the changes in the $CrPS_4$ layer during the RS process, we compared the crystallinity of the $CrPS_4$ layer in each state (Fig. 3d–f). The HRTEM image and its fast Fourier transform (FFT) pattern show that the $CrPS_4$ layer in the initial state was a single crystal, despite Ag atoms infiltrating from the interface. In addition, the Ag atoms did not form solid-state phases in the $CrPS_4$ layer (Fig. 3d). Unlike samples in the other states, the LRS sample featured additional spots in the FFT pattern (Fig. 3e), which matched the patterns of the Ag and Ag_2O phases (Supporting Information, Figure S5). The $CrPS_4$ layer in the LRS retained its crystallinity despite the existence of solid-state phases (including Ag) in the $CrPS_4$ layer. The observed Ag phases indicated that the Ag CFs consisted of crystalline phases. In the HRTEM image obtained for a $CrPS_4$ layer in the HRS (Fig. 3f), the Ag phase was removed, and the $CrPS_4$ retained a single-crystalline phase. The $CrPS_4$ layer could maintain its single-crystalline structure during RS induced by electrical stimulation, regardless of the presence of Ag phases.

To compare the breakdown state with other states, we applied +10 V (exceeding the value of SET voltage) to a Au/Ag/$CrPS_4$/Au device, which made the device metallic (Supporting Information, Figure S6). STEM and EDS data obtained after the breakdown process revealed that Ag atoms also accumulated near the Ag/$CrPS_4$ interface and formed many thick filaments distributed evenly in the $CrPS_4$ layer. In the breakdown state, the concentration of Ag was higher than that in the LRS, and the ratios of P and S compared with Cr were decreased to 1:0.5:2.1 (Cr:P:S). These results implied that the device was nonfunctional at high Ag concentration, accompanied by a decrease in P and S. Furthermore, a large current flow is known to cause Joule heating, which causes physical damage, interferes with device operation, and can even induce complete device breakdown.

It is noticeable that the shape of the CFs formed inside $CrPS_4$ differed from the conical CFs formed inside the general vertical devices reported in previous studies[35–37]. Because the Ag atoms (migrated into $CrPS_4$ in the initial state) can function as seeds for CF growth, the CFs formed inside the $CrPS_4$ showed dendrite structures near the upper interface. The migration of Ag appeared to be guided by S vacancies, with the CFs most likely growing along with them. The presence of these S vacancies can lead to stable switching phenomena; this is analogous to the case of defects and grain boundaries, which have previously been introduced to control CF growth and

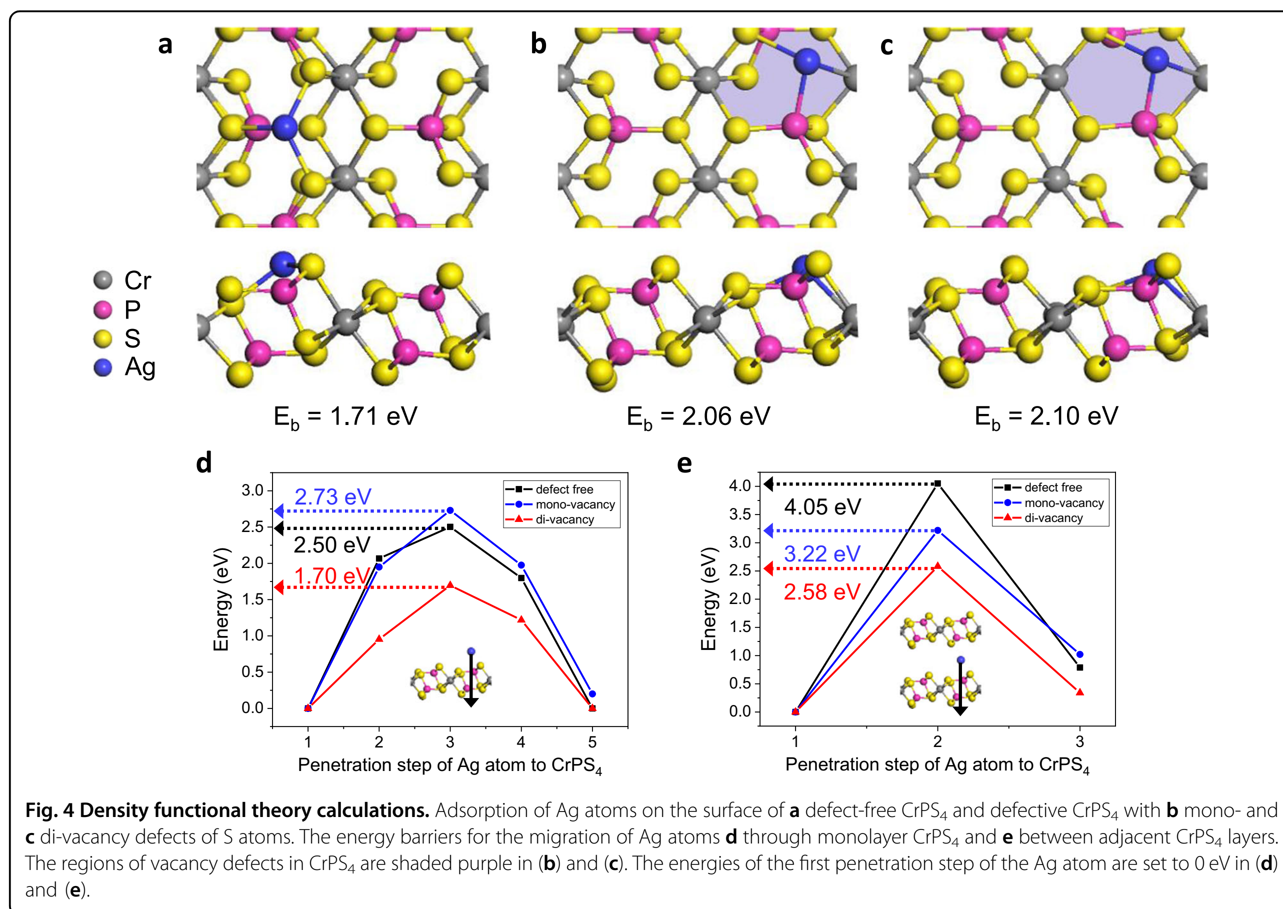

Fig. 4 Density functional theory calculations. Adsorption of Ag atoms on the surface of **a** defect-free $CrPS_4$ and defective $CrPS_4$ with **b** mono- and **c** di-vacancy defects of S atoms. The energy barriers for the migration of Ag atoms **d** through monolayer $CrPS_4$ and **e** between adjacent $CrPS_4$ layers. The regions of vacancy defects in $CrPS_4$ are shaded purple in (**b**) and (**c**). The energies of the first penetration step of the Ag atom are set to 0 eV in (**d**) and (**e**).

reduce its randomness[38]. Ag ion migration through S vacancies within a single-crystalline 2D material can reduce the randomness of CF growth and thus improve the durability, uniformity, and reliability of the device. Furthermore, the implementation of high-performance devices operating at low operating voltages is expected to become possible if defects are controlled. It was confirmed that the forming voltage of the Ag/$CrPS_4$/Au device could be reduced by controlling defects within $CrPS_4$ using a reactive ion etching process (Supporting Information, Figure S7).

To verify our hypothesis of Ag migration during the switching process and to explain the formation of Ag CFs inside the $CrPS_4$ layer, we performed spin-polarized density functional theory (DFT) calculations. In particular, we investigated the penetration of Ag atoms into $CrPS_4$ with and without vacancy defects. It was previously reported that Cu atoms easily pass through graphene containing enlarged vacancy defects[39]. Thus, we considered mono- and divacancy defects of S atoms in $CrPS_4$ to show the relationship between the penetration of Ag atoms and the sizes of vacancy defects in $CrPS_4$. First, we studied the binding behaviors of Ag atoms on the surface of monolayer $CrPS_4$ with and without vacancy defects. Figure 4 shows the adsorption of an Ag atom on (a) defect-free $CrPS_4$ and defective $CrPS_4$ with (b) mono- and (c) di-vacancy defects of S atoms. We obtained the binding energy (E_b) per surface unit cell using the following equation: $E_b = -\{E_{Ag/CrPS_4} - (E_{CrPS_4} + E_{Ag})\}$, where $E_{Ag/CrPS_4}$, E_{CrPS_4}, and E_{Ag} are the total energies of Ag-adsorbed $CrPS_4$, isolated $CrPS_4$, and a single Ag atom, respectively. We observed that the Ag atom had a larger E_b (by ~0.4 eV) on defective $CrPS_4$ with mono- or divacancy defects than on defect-free $CrPS_4$, as shown in Fig. 4. This suggested that Ag atoms tend to be adsorbed on defective $CrPS_4$ rather than on defect-free $CrPS_4$. To study the penetration of Ag atoms into $CrPS_4$ (as a function of the size of vacancy defects), we obtained the energy barriers for the migration of Ag atoms through monolayer $CrPS_4$ by using nudged elastic band (NEB) calculations. In Fig. 4d, the first penetration step indicates the atomic configuration of the Ag atom adsorbed on the $CrPS_4$ surface shown in Fig. 4a–c. Our calculations revealed that the Ag atom has the lowest energy barrier (of 1.70 eV) when passing through the surface of defective $CrPS_4$ with divacancy S defects compared to the cases of defect-free $CrPS_4$ and defective $CrPS_4$ with monovacancy S defects. However, despite the vacancy defects in $CrPS_4$,

the Ag atom on $CrPS_4$ with monovacancy defects had a larger energy barrier than that on defect-free $CrPS_4$ due to its strong binding behavior on the surface of $CrPS_4$ with monovacancy defects. The energy barrier of Ag atoms was significantly decreased on $CrPS_4$ with divacancy defects due to the ample space inside the $CrPS_4$. Figure 4e shows the energy barrier for the migration of Ag atoms between adjacent $CrPS_4$ layers. The lowest-energy barrier between adjacent $CrPS_4$ layers with divacancy defects was obtained for the migration of Ag atoms. This indicated that Ag atoms could more easily pass through $CrPS_4$ as the size of vacancy defects increased and that they tended to move along the vacancy defect sites inside the $CrPS_4$ layers.

Conclusion

In summary, we analyzed the mechanism behind the RS behavior of ECM devices using $CrPS_4$ (an emerging 2D insulator) as an electrolyte. TEM measurements revealed that the RS behaviors of ECM devices were caused by the formation and rupture of CFs composed of Ag atoms infiltrating into the $CrPS_4$ layer. It was confirmed that the $CrPS_4$ layers retained their single-crystalline structures, while Ag atoms migrated through the $CrPS_4$ layers, leading to the formation and rupture of the CFs. DFT calculations demonstrated that Ag atoms migrated more readily through defective $CrPS_4$ layers with S divacancy defects than through defect-free $CrPS_4$ layers or defective $CrPS_4$ layers with S monovacancy defects. These results showed that cations can migrate within a 2D layered single-crystalline material electrolyte in an ECM device structure, and the two-dimensionally confined properties of the material can thereby be utilized to enhance the durability, uniformity, and reliability of the device.

Acknowledgements

This work was supported by a National Research Foundation of Korea (NRF) grant funded by the Korean government (MSIP) (No. 2013R1A3A2042120), the Nano Material Technology Development Program through the NRF funded by the MSIP (No. 2016M3A7B4909668), and the KIST R&D program (2V06990). The work at Sejong University was supported by the Global Research and Development Center Program (2018K1A4A3A01064272), Basic Science Research Program (2017R1A2B2010123) through the NRF funded by the Ministry of Science and ICT (MSIT), and Priority Research Center Program (2010-0020207) through the NRF funded by the Ministry of Education (MOE). The work at the IBS CCES and SNU was supported by the Institute for Basic Science (IBS) in Korea (Grant No. IBS-R009-G1).

Author details

[1]Department of Physics, Konkuk University, Seoul 05029, Korea. [2]Advanced Analysis Center, Korea Institute of Science and Technology, Seoul 02792, Korea. [3]Department of Materials Science and Engineering, Korea University, Seoul 02841, Korea. [4]Department of Physics, Graphene Research Institute, and GRI-TPC International Research Center, Sejong University, Seoul 05006, Korea. [5]Center for Correlated Electron Systems, Institute for Basic Science, Seoul 08826, Korea. [6]Department of Physics and Astronomy, Seoul National University, Seoul 08826, Korea

Conflict of interest

The authors declare that they have no conflict of interest.

Publisher's note

Springer Nature remains neutral with regard to jurisdictional claims in published maps and institutional affiliations.

Supplementary information is available for this paper at https://doi.org/10.1038/s41427-020-00272-x.

Received: 15 July 2020 Revised: 13 October 2020 Accepted: 22 October 2020.
Published online: 18 December 2020

References

1. Sawa, A. Resistive switching in transition metal oxides. *Mater. Today* **11**, 28–36 (2008).
2. Waser, R. & Aono, M. Nanoionics-based resistive switching memories. *Nat. Mater.* **6**, 833–840 (2007).
3. Waser, R., Dittmann, R., Staikov, C. & Szot, K. Redox-based resistive switching memories nanoionic mechanisms, prospects, and challenges. *Adv. Mater.* **21**, 2632–2663 (2009).
4. Hasegawa, T., Terabe, K., Tsuruoka, T. & Aono, M. Atomic switch: atom/ion movement controlled devices for beyond von-Neumann computers. *Adv. Mater.* **24**, 252–267 (2012).
5. Yang, J. J., Strukov, D. B. & Stewart, D. R. Memristive devices for computing. *Nat. Nanotechnol.* **8**, 13–24 (2013).
6. Valov, I., Waser, R., Jameson, J. R. & Kozicki, M. N. Electrochemical metallization memories—fundamentals, applications, prospects. *Nanotechnology* **22**, 289502 (2011).
7. Celano, U. et al. Three-dimensional observation of the conductive filament in nanoscaled resistive memory devices. *Nano Lett.* **14**, 2401–2406 (2014).
8. Celano, U. et al. Understanding the dual nature of the filament dissolution in conductive bridging devices. *J. Phys. Chem. Lett.* **6**, 1919–1924 (2015).
9. Strukov, D. B., Snider, G. S., Stewart, D. R. & Williams, R. S. The missing memristor found. *Nature* **453**, 80–83 (2008).
10. Edwards, A. H. et al. Reconfigurable memristive device technologies. *Proc. IEEE* **103**, 1004–1033 (2015).
11. Borghetti, J. et al. 'Memristive' switches enable 'stateful' logic operations via material implication. *Nature* **464**, 873–876 (2010).
12. Lu, W., Kim, K. H., Chang, T. & Gaba, S. Two-terminal resistive switches (memristors) for memory and logic applications. *Proc. Asia South Pacific Des. Autom. Conf. ASP-DAC* 217–223 (2011).
13. Doo, S. J., Kim, I., Ziegler, M. & Kohlstedt, H. Towards artificial neurons and synapses: a materials point of view. *RSC Adv.* **3**, 3169–3183 (2013).
14. Suri, M. et al. CBRAM devices as binary synapses for low-power stochastic neuromorphic systems: auditory (Cochlea) and visual (Retina) cognitive processing applications. *Tech. Dig. - Int. Electron Devices Meet. IEDM* 10.3.1–10.3.4 (2012).
15. Ohno, T. et al. Short-term plasticity and long-term potentiation mimicked in single inorganic synapses. *Nat. Mater.* **10**, 591–595 (2011).
16. Li, S. et al. Synaptic plasticity and learning behaviours mimicked through Ag interface movement in an Ag/conducting polymer/Ta memristive system. *J. Mater. Chem. C.* **1**, 5292–5298 (2013).
17. Yang, Y. et al. Electrochemical dynamics of nanoscale metallic inclusions in dielectrics. *Nat. Commun.* **5**, 4232 (2014).
18. Zhang, Z. et al. Electrochemical metallization cell with solid phase tunable $Ge_2Sb_2Te_5$ electrolyte. *Sci. Rep.* **8**, 12101 (2018).
19. Ge, R. et al. Atomristor: nonvolatile resistance switching in atomic sheets of transition metal dichalcogenides. *Nano Lett.* **18**, 434–441 (2018).
20. Rehman, S. et al. Thickness-dependent resistive switching in black phosphorus CBRAM. *J. Mater. Chem. C.* **7**, 725–732 (2019).
21. Bessonov, A. A. et al. Layered memristive and memcapacitive switches for printable electronics. *Nat. Mater.* **14**, 199–204 (2015).
22. Lee, M. J. et al. Synaptic devices based on two-dimensional layered single-crystal chromium thiophosphate ($CrPS_4$). *NPG Asia Mater.* **10**, 23–30 (2018).
23. Qian, K. et al. Hexagonal boron nitride thin film for flexible resistive memory applications. *Adv. Funct. Mater.* **26**, 2176–2184 (2016).
24. Pan, C. et al. Coexistence of grain-boundaries-assisted bipolar and threshold resistive switching in multilayer hexagonal boron nitride. *Adv. Funct. Mater.* **27**, 1604811 (2017).
25. Kohn, W. & Sham, L. J. Self-consistent equations including exchange and correlation effects. *Phys. Rev.* **140**, A1133–A1138 (1965).

26. Perdew, J. P., Burke, K. & Ernzerhof, M. Generalized gradient approximation made simple. *Phys. Rev. Lett.* **77**, 3865–3868 (1996).
27. Kresse, G. & Furthmüller, J. Efficient iterative schemes for ab initio total-energy calculations using a plane-wave basis set. *Phys. Rev. B - Condens. Matter Mater. Phys.* **54**, 11169–11186 (1996).
28. Kresse, G. & Furthmüller, J. Efficiency of ab-initio total energy calculations for metals and semiconductors using a plane-wave basis set. *Comput. Mater. Sci.* **6**, 15–50 (1996).
29. Blöchl, P. E. Projector augmented-wave method. *Phys. Rev. B* **50**, 17953–17979 (1994).
30. Joubert, D. From ultrasoft pseudopotentials to the projector augmented-wave method. *Phys. Rev. B - Condens. Matter Mater. Phys.* **59**, 1758–1775 (1999).
31. Grimme, S., Antony, J., Ehrlich, S. & Krieg, H. A consistent and accurate ab initio parametrization of density functional dispersion correction (DFT-D) for the 94 elements H-Pu. *J. Chem. Phys.* **132**, 154104 (2010).
32. Joe, M. et al. A comprehensive study of piezomagnetic response in $CrPS_4$ monolayer: mechanical, electronic properties and magnetic ordering under strains. *J. Phys. Condens. Matter* **29**, 405801 (2017).
33. Zhuang, H. L. & Zhou, J. Density functional theory study of bulk and single-layer magnetic semiconductor $CrPS_4$. *Phys. Rev. B* **94**, 195307 (2016).
34. Jiang, L., Lv, F. C., Yang, R., Hu, D. C. & Guo, X. Forming-free artificial synapses with Ag point contacts at interface. *J. Mater.* **5**, 296–302 (2019).
35. Chen, J. Y., Huang, C. W., Chiu, C. H., Huang, Y. T. & Wu, W. W. Switching kinetic of VCM-based memristor: evolution and positioning of nanofilament. *Adv. Mater.* **27**, 5028–5033 (2015).
36. Cho, B. et al. Direct observation of Ag filamentary paths in organic resistive memory devices. *Adv. Funct. Mater.* **21**, 3976–3981 (2011).
37. Kwon, D.-H. et al. Atomic structure of conducting nanofilaments in TiO_2 resistive switching memory. *Nat. Nanotechnol.* **5**, 148–153 (2010).
38. Choi, S. et al. SiGe epitaxial memory for neuromorphic computing with reproducible high performance based on engineered dislocations. *Nat. Mater.* **17**, 335–340 (2018).
39. Zhao, Y. et al. Mass transport mechanism of Cu species at the metal/dielectric interfaces with a graphene barrier. *ACS Nano* **8**, 12601–12611 (2014).